Chemical Engineering Journal 471 (2023) 144560

Contents lists available at ScienceDirect

Chemical Engineering Journal

journal homepage: www.elsevier.com/locate/cej

Hierarchical diffusion pathways into VOC adsorption films by direct ink writing and ammonium carbonate treatment

Qiwei Chen [b], Zhuo Chen [b], Yan Wang [b], Enze Tian [c,d], Jinhan Mo [a,b,e,f,*]

[a] College of Civil and Transportation Engineering, Shenzhen University, Shenzhen 518060, China
[b] Beijing Key Laboratory of Indoor Air Quality Evaluation and Control, Department of Building Science, Tsinghua University, Beijing 100084, China
[c] Songshan Lake Materials Laboratory, Dongguan 523808, China
[d] Institute of Physics, Chinese Academy of Sciences, Beijing 100190, China
[e] Key Laboratory of Coastal Urban Resilient Infrastructures (Shenzhen University), Ministry of Education, Shenzhen 518060, China
[f] Key Laboratory of Eco Planning & Green Building (Tsinghua University), Ministry of Education, Beijing 100084, China

ARTICLE INFO

Keywords:
Direct ink writing
Rheological behaviour
Hierarchical porous structure
Diffusion kinetics
Indoor air quality

ABSTRACT

In-situ thermally restorable adsorption films exhibited brilliant performance for indoor volatile organic compounds (VOCs) purification with negligible wind resistance and considerable lifetime. However, the morphology of adsorption films should be restructured for better adsorption kinetics. This study structured adsorption films with submillimeter-sized channels by direct ink writing (DIW). Submicron-micron-sized porous structure was further fabricated through ammonia carbonate treatment. Pore size distribution characterization proved 33% of extra mesopores were created in the hierarchical porous adsorption film. Dynamic adsorption behaviours for formaldehyde and toluene illustrated that the hierarchical porous adsorption film exhibited an over 80% initial one-pass efficiency for both formaldehyde and toluene, improved by 20% over the plane adsorption film. The purification rate was also significantly improved by 83% and 67% for formaldehyde (from 0.059 mg $g^{-1}h^{-1}$ to 0.106 mg $g^{-1}h^{-1}$) and toluene (from 0.143 mg $g^{-1}h^{-1}$ to 0.239 mg $g^{-1}h^{-1}$), respectively. This study proposed a method for conveniently preparing multi-scale porous structured adsorption components under mild conditions. The hierarchical diffusion pathways induced by DIW and ammonium carbonate treatment will enhance the adsorption kinetics and the purification performance of the adsorption film, overcoming the weak purification performance and short material lifetime of the existing indoor VOCs adsorption components. This research can be further applied to gas separation, as well as gas sensing, as DIW can achieve sub-millimeter scale resolution, providing a versatile approach for heat and mass transfer enhancement in chemical and environmental fields.

1. Introduction

Indoor volatile organic compounds (VOCs), such as formaldehyde and toluene, can cause chronic damage to human bodies for even decades [1] due to their continuous emission from massive indoor chemical sources like furniture [2,3] and decoration coatings [4], increasing the risk of severe illness [5-8]. Adsorption has been exploited extensively for gaseous pollutants removal [9] as it is economical [10] and by-products free [11]. If the adsorption component is appropriately designed, adsorption can efficiently remove VOCs at low concentrations [12,13].

Traditional powder adsorbent is easy to prepare and can maintain the maximum specific surface area and the highest adsorption capacity of the material. However, the powder-filled adsorption component will be very dense, leading to a large flow resistance, limiting its practical application. As far as we know, the powder-filled adsorption component can only be used as a fluidized bed in chemical engineering [14,15]. Adsorbents shaped by granulation are commonly used in residential or industrial purification equipment [16,17], even rare suitable [18,19], facing formidable challenges of high air resistance and poor flexibility. In addition, bad adsorption kinetics [20,21] will restrict the efficiency and adsorption amount of materials and increase the cost of maintenance and the replacement of materials. Structured monolithic adsorption components have been studied more and more extensively [22,23]. Their hierarchical porous architecture consisting of macro-channels, intrinsic nanopores and large surface areas enables a lower pressure drop and better mass transfer kinetics compared with granular materials [24,25]. Traditionally, monoliths are fabricated by hydraulic or screw

* Corresponding author.
E-mail addresses: mojinhan@szu.edu.cn, mojinhan@tsinghua.edu.cn (J. Mo).

https://doi.org/10.1016/j.cej.2023.144560
Received 13 April 2023; Received in revised form 27 June 2023; Accepted 30 June 2023
Available online 1 July 2023

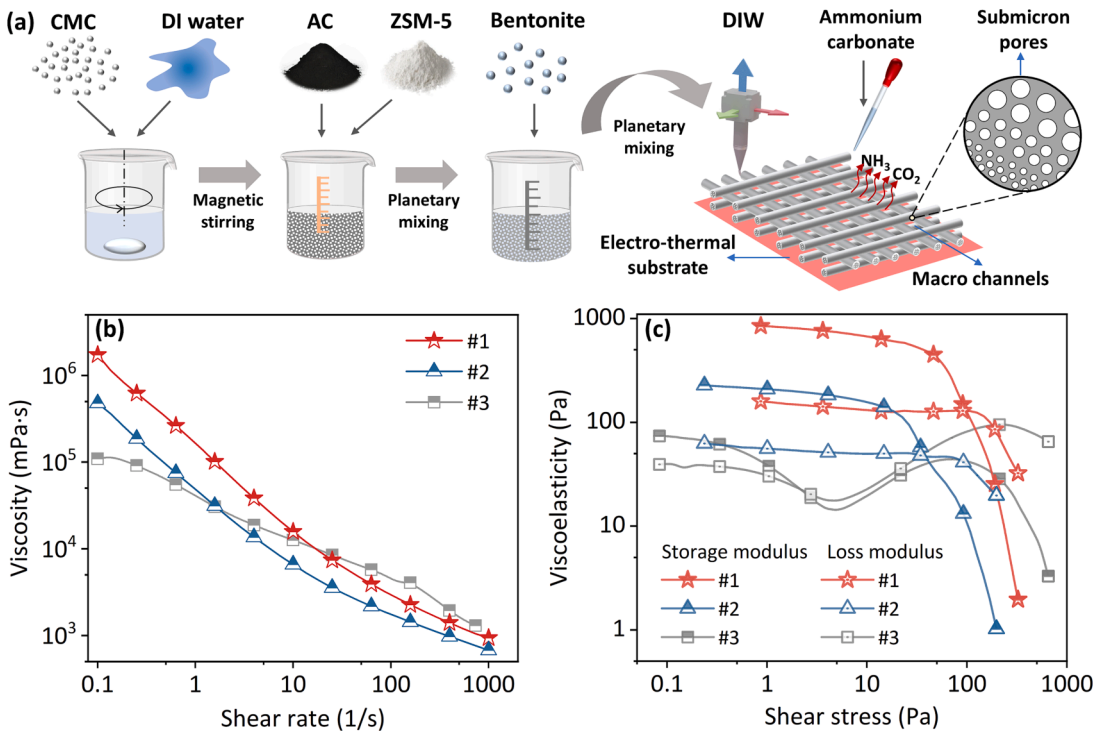

Fig. 1. (a) Preparations of the printing inks and the adsorption films with hierarchical porous structures. The viscosities (b) and viscoelasticities (c) of Inks #1, #2, and #3.

extrusion techniques [26,27]. However, the geometry of extruded monoliths is highly dependent on sophisticated moulds, which brings extra labour, equipment, and time and limits the geometric degree of freedom and material versatility of the adsorbents.

Direct ink writing (DIW) has been used for preparing gas-phase adsorption components [28-31]. Generally, the semi-liquid adsorbent ink of high solid loading ratios exhibits a shear-thinning rheological property, making shape retention possible after printing [32,33]. A wide variety of adsorbents [34,35], such as carbon adsorbents, zeolites, MOFs and COFs, can be adapted to DIW fabrication if supplemented with appropriate binders and plasticizers [36,37]. Grande et al. [38] prepared a non-aqueous ink and printed a MOF monolith for carbon dioxide, moisture, nitrogen and methane adsorption. Middelkoop et al. [39] fabricated porous-carbon monoliths for carbon dioxide capture via DIW. Some studies applied DIW-fabricated adsorption components for VOCs removal [40-43]. Wang et al. printed a monolith of ZSM-5 core and silicalite-1 shell by DIW for good mass transfer kinetics, and the silicalite-1 shell was hydrophobic to avoid the competitive adsorption of moisture [43]. Results show that the breakthrough time of the adsorption monolith for toluene is 580 s under 5% relative humidity and 430 s under 50% relative humidity. Scott et al. [44] printed activated carbon-based honeycomb-like adsorption components with millimetre-sized channels for butane adsorption. Breakthrough experiments showed that the printed adsorption component owns an over 40-min lifetime, around 4 times as long as the commercial packed bed column. Zhao et al. printed silica aerogels containing MnO_2 spheres as catalysts for ppm-level toluene photocatalytic degradation during thermal transpiration [45]. Within 6 h, the silica-MnO_2 monolith can decompose 18 ppm toluene to less than 4 ppm. Lawson et al. [46] printed an adsorption monolith component of metal oxide and H-ZSM-5 for n-hexane adsorption and catalytic cracking. Results showed the Cr-doped H-ZSM-5 monolith presented 85% n-hexane conversion and showed no deactivation after 6 h adsorption and catalytic reactions. Zhang et al. [47] printed a polymer monolith with intrinsic microporosity (PIM-1). The macroporosity induced by DIW and the intrinsic microporosity enable PIM-1 to fully purify toluene vapor for 1.7 h, and the breakthrough can be as long as 5.6 h. The VOCs removal performances (e.g. efficiency, breakthrough time) of the existed DIW fabricated porous adsorption components have been very good, but the experimental air flowrate or face velocity are usually not applicable for practical use [44,47].

However, the exacting requirements of the rheological property for the DIW ink bring challenges to some brilliant adsorbents, including MOFs and activated carbon (AC), which are highly efficient for VOCs adsorption [48]. For example, AC is difficult to be dispersed evenly in ink, especially in aqueous ink, resulting in poor rheological properties [49]. Adding more binders or easy-to-disperse adsorbents (i.e. zeolite powder) to the ink could improve the rheological properties [39,49]. Regufe et al. mixed zeolite 13X and conductive porous carbon to prepare an aqueous ink with better rheological properties than porous carbon alone, as zeolite 13X was uniformly mixed with AC, promoting its dispersion property and hydrophilicity [49].

The flexibility and great freedom enable DIW to automate the moulding of materials to adsorption components with superior mass transfer kinetics, such as honeycomb-like adsorption monoliths [43] and the trough-like finned adsorption board [40]. The adsorption structures with sub-millimetre resolution enable adequate contact between the adsorbent and VOCs, and provide a much shorter diffusion pathway for the VOC molecules into the adsorbent, accelerating the VOC capture rate. However, VOCs still diffuse slowly through the intrinsic nanopores into the carbon material [50]. If more micron-sized pores were formed, the interconnected hierarchical porous structures would further accelerate the inward diffusion rate [51]. Thus, VOC removal efficiency in the initial adsorption period can be improved.

Due to the limitation of the DIW resolution, the submicron-micron-sized structures need extra auxiliary methods. Gas emulsion and sacrificial template methods have been applied to fabricate submicron-micron porous structures in recent years [52-56]. Zhao et al. fabricated a silicone rubber membrane with ordered micropores through solvent evaporation-induced phase separation [57]. Uniform 10 μm – 20 μm pores are synthesized, which is attributed to the nucleation, growth, and coalescence process of liquid paraffin in the rubber membrane. Liu et al. printed hierarchical porous Al2O3 ceramic lattices by

DIW assisted with gel emulsion [58]. The stable gel emulsion acted as a liquid sacrificial template, forming a hierarchical porous structure by heating. Huang et al. synthesized micron-sized pores in a monolith by decomposing preadded polymethyl methacrylate beads (as a sacrificial template) under high temperatures [59]. The content and size of the template particles were adjusted to prepare porous structures with different pore sizes and porosities. Liu et al. fabricated micron-sized pores using a similar method, and the porous networks accelerated the matter transport in dye degradation reactions [60]. Compared with the high-temperature calcination required in the above preparation process, developing novel methods of micron-sized pore preparation under milder conditions may be more applicable in indoor VOC removal.

In this study, a sub-millimeter net-like adsorption film with an interconnected hierarchical porous structure was prepared via DIW. AC was exploited as the adsorbent as it has performed great adsorption performance for many VOCs in indoor environments and has been a very commonly used adsorbent for VOCs removal [12,61]. and ZSM-5 zeolite, having similar physical properties to zeolite 13X, was added as the co-adsorbent to modify the rheological properties of the ink. Ammonium carbonate was used to evaporate ammonia gas and carbon dioxide to form micron-sized pores. Thus, the inward VOC diffusion rate of the adsorption film could be accelerated. The adsorption film was coated on a temperature-adjustable substrate first proposed by Chen et al. [62] to realize rapid *in-situ* desorption after the adsorbent got saturated. Formaldehyde and toluene purification experiments were conducted, and the ammonium carbonate processed net-like adsorption film exhibited great VOC adsorption and regeneration performances. The adsorption films with hierarchical porous structures proposed in this study will provide a solution for long-term indoor VOC removal and broaden the horizons of gas-phase adsorption applications, including gas separation and carbon capture.

2. Experimental section

2.1. Materials

Activated carbon (AC) and ZSM-5 zeolite were purchased from Jiangsu XFNANO Co., Ltd. Carboxymethyl cellulose (CMC) and ethylene–vinyl acetate (EVA) copolymer were provided by Topg Health Technology (Guangdong) Co., Ltd. Bentonite clay as a binder was purchased from Beijing Merida Technology Co., Ltd. Ammonium carbonate was purchased from Shanghai Aladdin Biochemical Technology Co., Ltd.

2.2. Ink preparation

Fig. 1 (a) presents the preparation of inks. First, 2 g CMC was dissolved in 98 g deionized water at 80 °C with sufficient stirring at 600 r min^{-1} for 1 h by a magnetic stirring apparatus (Corning PC-420D) to get a well-dispersed viscous suspension. Then 20 g suspension and 9 g deionized (DI) water were added to a powder mixture consisting of 11 g ZSM-5 and 5.5 g AC, which had been thoroughly stirred through a planetary ball mill (QM-QX04, NJU Instrument Co., Ltd.). ZSM-5 was added to the printing ink to adjust the ink rheology, as AC has poor dispersion and rheological properties. Then, a planetary mixer (IGT SimplyMix Mixer) stirred the mixture for 2 min (revolution speed, 3600 r min^{-1}; self-rotation speed, 800 r min^{-1}) to get a uniform dispersion. Bentonite and EVA were both tried as binders. Four g bentonite was added to the dispersion as a binder, followed by 2 min stirring by the planetary mixer to prepare a uniform solid-like Ink #1. While for EVA, 4 g bentonite was replaced by 2 g EVA, and other operations remained the same to get Ink #2. Ink #3 was also prepared without any binders for comparison.

2.3. Rheological property tests

The viscosity and viscoelasticity of Inks #1, #2 and #3 were tested on a rotational rheometer (MCR 302, Anton-Paar Instruments) using a parallel plate measuring system at 24 °C. For the viscosity test, the shear rate was uniformly changed from 0.1 s^{-1} to 1000 s^{-1}. For the viscoelasticity test, the shear strain was uniformly changed from 0.1% to 1000%. The inks with suitable rheological properties would be used for further study.

2.4. Preparation methods of the printing inks and the adsorption films with hierarchical porous structures

The ink was loaded in a bio-printer (Eazao, Bio), as shown in Fig. 1 (a). The models of adsorption films were designed with Solidworks 2019, and converted to G-codes that determine the printing pathways by Ultimaker Cura 4.11.0. Two types of adsorption films with different morphologies were printed on the electrothermal PI circuit substrates by DIW, which were the plane adsorption film (PAF) and the net-like adsorption film (NAF, adsorption film composed of mutually perpendicular material filaments, as shown in Fig. 1 (a)). During the printing process, 10 g 2 mol L^{-1} ammonium carbonate solution was dropped on the annealed PAF and NAF to fabricate PAF@N and NAF@N, respectively. Then four kinds of adsorption films were dried in an oven (DZF-6050, Shanghai Jinghong) for 2 h at 120 °C. The adsorption films were easily peeled off from the PI circuit substrate and later quickly annealed at 500 °C for 1 h under high-purity argon gas flow with a rapid annealing furnace (As-One RTP System, Annealsys). A thermogravimetric analysis (TGA) was conducted to monitor the content variation of the adsorption film caused by the annealing treatment. Then PAF, NAF, PAF@N and NAF@N were coated on a temperature-adjustable PI circuit substrate [63] with EVA copolymer for further gas adsorption experiments.

2.5. Chemical and morphological characterization

The size and morphology of the raw adsorbents and printed films were tested by a field emission scanning electron microscopy (FE-SEM, ZEISS MultiSEM 505). The elemental composition and distribution spectrograms of adsorbents before and after printing were analyzed by an energy-dispersive spectrometer (EDS, ZEISS MultiSEM 505). The specific surface area (SSA) was estimated by the Brunauer, Emmett and Teller (BET) method. The pore size distribution (PSD) was measured by the Density Functional Theory (DFT) method and Barret Joyner Halenda (BJH) method. The adsorption behaviours of the fabricated adsorption films and the raw adsorbents were evaluated by isothermal N_2 adsorption experiments. The chemical groups of NAF before and after ammonium carbonate treatment were detected by Fourier Transform infrared spectrometer (FTIR, Nicolet 6700FTIR).

2.6. Dynamic adsorption experiments and thermal regeneration

The annealed adsorption films were fixed on an air passage (450 mm × 70 mm × 3 mm), where the dynamic adsorption experiments were conducted. A microfluidic controlled gas evaporation generator [40] was used to generate formaldehyde and toluene stably. The ambient air was filtered by a high-efficiency particulate air (HEPA) filter and purified by activated carbon packed pipe in sequence, subsequently pumped into a spiral stainless-steel tube inside a sealed oil tank with a heating control. The heated air purged the evaporated gas from the generator to form polluted air with a stable concentration of the target pollutant. The pollutant flow passed over the adsorption film that had been fixed in the air passage and got adsorbed. The airflow rate was maintained at 3.6 L min^{-1} by a mass flow controller (MC 20SLPM, Alicat Scientific, USA) with a residence time of 0.13 s. The formaldehyde and toluene concentrations in the air before and after the adsorption film (C_{in} and C_{out}) were monitored using a gas chromatography - barrier ionization discharge (GC-BID) detector (Shimazu, Nexis GC2030-BID) and a VOC detector (Honeywell, ppbRAE3000 PGM-7340) in a controlled environment (23.0 ± 1.0 °C, 25% ± 5% relative humidity), respectively.

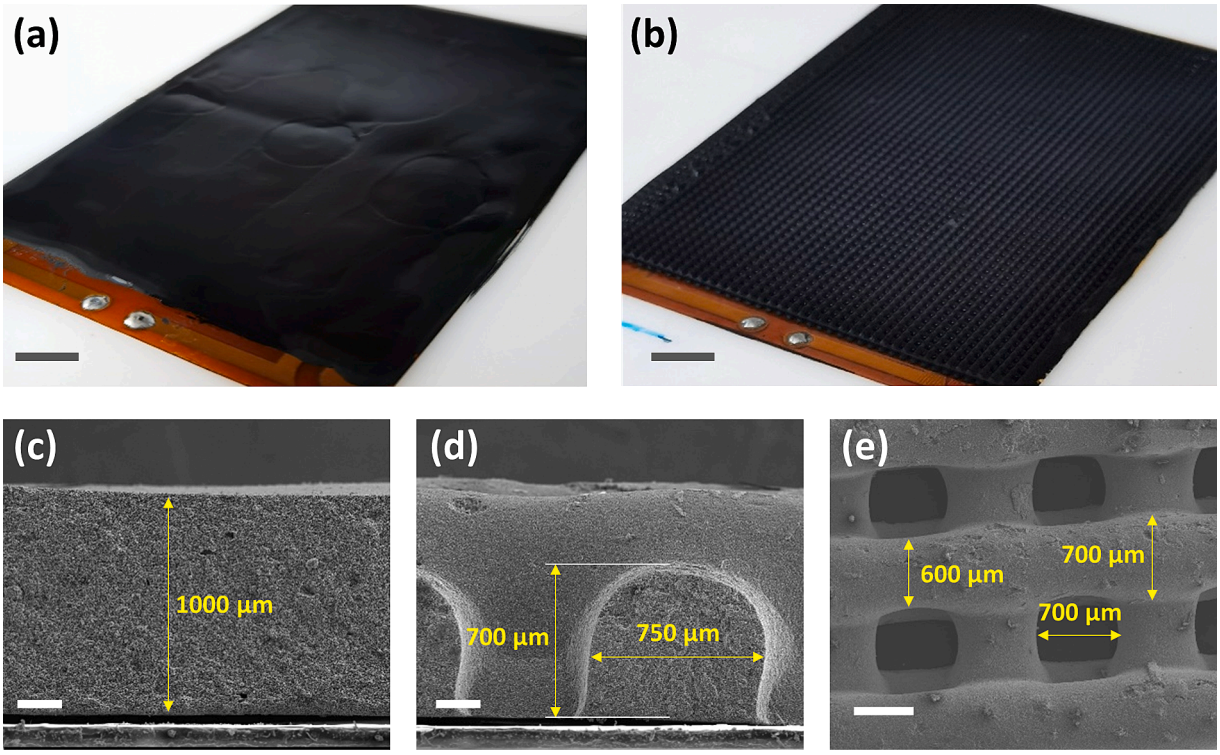

Fig. 2. Images of (a) PAF and (b) NAF. The SEM images from the cross-section of (c) PAF and (d) NAF. (e) The SEM image from the top view of NAF. Scale bars, 1 cm for (a) and (b), 200 μm for (c) and (d), and 500 μm for (e). PAF@N and NAF@N have almost the same appearance as PAF and NAF, respectively.

XRD and XPS characterizations were conducted on the adsorbents before and after formaldehyde and toluene adsorption to ensure the stability of the adsorption films during the adsorption of formaldehyde and toluene. Following the adsorption performance decayed, *in-situ* electrothermal regeneration was conducted by applying a direct current (DC) regulated power supply (20 V, 24 W) to the PI circuit substrate to control the adsorbent temperature at 80 °C for formaldehyde regeneration and 100 °C for toluene regeneration. The temperature increase process could finish in less than one minute [64].

3. Results and discussion

3.1. Rheological properties of the inks

Fig. 1 (b) shows the viscosities of Inks #1−#3. Three inks all present shear-thinning rheology, meaning the viscosity decreases as the shear process accelerates. A high-quality 3D printing ink should have a relatively low viscosity at a rapid shear rate to ensure that the ink extrusion process from an ultra-thin nozzle proceeds smoothly and a relatively high viscosity at a low shear rate to prevent the extruded ink from flowing deformation. As the shear rate increases from 0.1 s^{-1} to 1000 s^{-1}, the viscosity of Ink #1 changes from 1.7 × 10^6 mPa s to 940 mPa s, the viscosity of Ink #2 changes from 4.8 × 10^5 mPa s to 680 mPa s, and the viscosity of Ink #3 changes from 1.1 × 10^5 mPa s to 1300 mPa s. Among the three inks, the viscosity curve of Ink #1 is steeper than Ink #2, while the viscosity variation of Ink #3 is the gentlest. In addition, the viscosity of Ink #1 is large enough to ensure that the resolution of DIW fabrication will not be reduced due to the flowing deformation of printed ink. Therefore, Ink #1 is the most suitable for DIW preparation.

The ink viscoelasticity was shown in Fig. 1 (c), including storage modulus (SM) and loss modulus (LM), which are essential parameters determining whether DIW can proceed successfully, and the quality of DIW molding. From Fig. 1 (c), the SMs of Inks #1 and #2 are both high at low shear stress and gradually decrease. Their LMs also decrease with the increase of shear stress, but the decay rate is lower than that of SM. Thus, SM is greater than LM under low shear stress. Under this condition, the elastic properties of the viscoelastic DIW ink will dominate; that is, the ink will behave like a solid and is not easy to deform at a low shear rate. While under high shear stress, SM is less than LM, and the viscous property of ink dominates, so the ink behaves like a liquid and has good fluidity at a high shear rate. Since the yield stress (the shear stress at the intersection of the SM curve and LM curve) of Ink #1 is greater than that of Ink #2, as the ink is extruded out and the shear stress generally decreases, Ink #1 exhibits solid material properties earlier. Hence its flowing deformation will not be as significant as Ink #2. The SM and LM curves of Ink #3 do not exhibit similar properties and may result in the failure of DIW molding. Due to the comprehensive consideration of viscosity and viscoelastic characteristics, Ink #1 was selected for the subsequent DIW preparation.

3.2. Morphologies and adsorption behaviours of DIW fabricated adsorption film

3.2.1. Surface morphology of adsorption films

Three adsorption structures are printed onto the temperature-controllable flexible PI substrates. The appearances of PAF and NAF are shown in Fig. 2 (a) and (b). PAF@N and NAF@N have almost identical appearances as PAF and NAF, respectively. It can be seen that the surface of PAF has uneven bumps due to the non-uniformity of the artificial paint-coating method. However, the surface of NAF is flat, and many mutually perpendicular adsorbent filaments form a uniform three-dimensional grid structure. Fig. 2 (c) and (d) show that the thickness of the two laminates is about 1 mm. Fig. 2 (d) and (e) clearly show the uniform net-like structure in the NAF, with a width of about 700 μm and a thickness of about 700 μm. The material filament in Fig. 2 (d) is slightly wider than 700 μm, as the underlying adsorbent filaments will slightly deform due to the pressure of the piled adsorbent on top. The thickness of the extruded adsorbent filament varies slightly according to the location (Fig. 2 (e)), because the extruded ink falling on the space between the underlying adsorbent filaments will be stretched due to

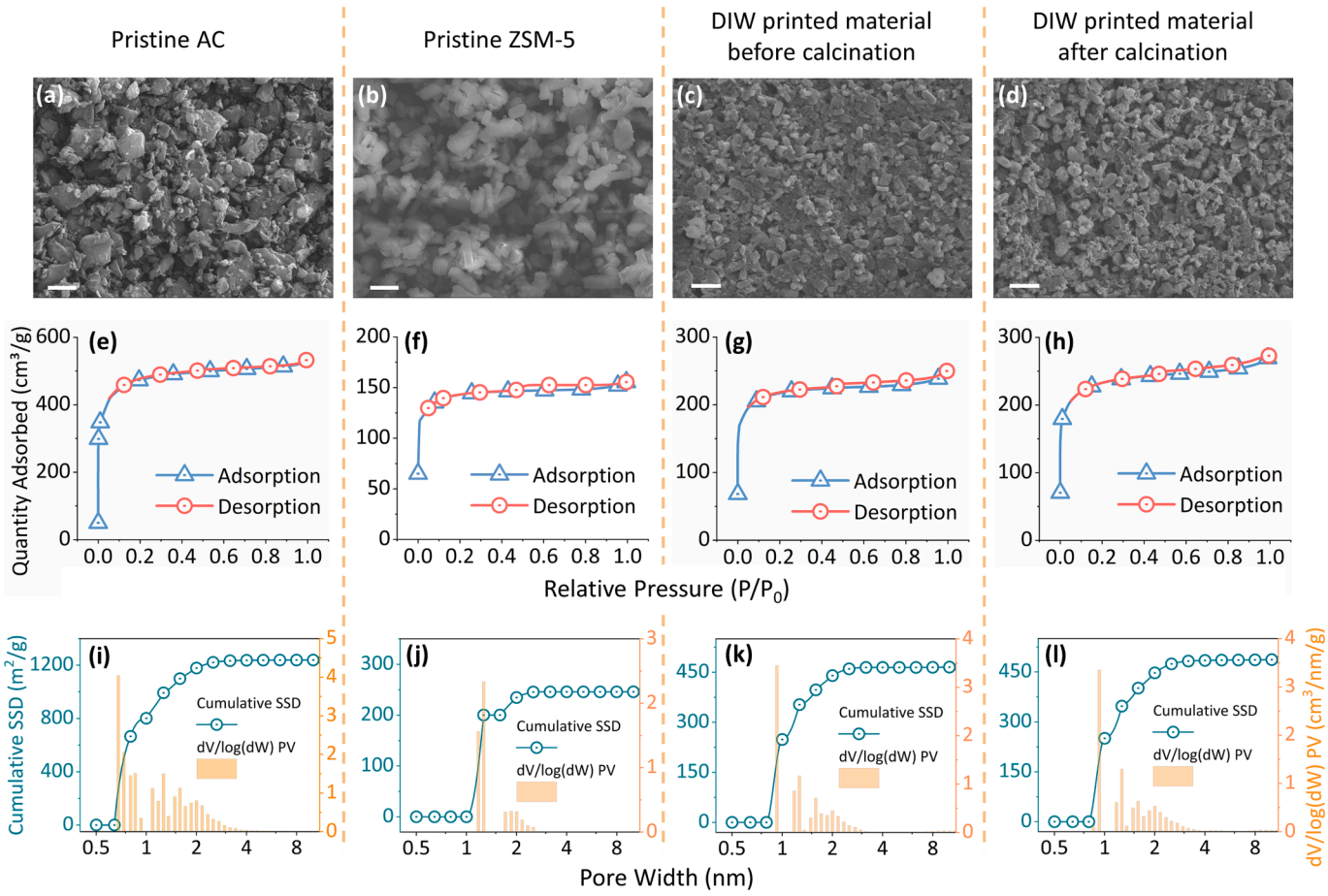

Fig. 3. SEM images of the microscopic morphologies of the pristine activated carbon (AC) (a) and ZSM-5 (b), scale bars, 5 μm; and the DIW fabricated material before calcination (c) and after calcination (d), scale bars, 10 μm. Figures (e) – (h) are the adsorption isothermals of materials (a) – (d), respectively. Figures (i) – (l) are the cumulative specific surface area (SSA) and the pore volume (PV) distribution over pore size (dV/log(dW) PV) of materials (a) – (d), respectively, carried out by static adsorption experiments with N_2 under 70 K. The SSA and pore size distribution (PSD) are estimated using the density functional theory (DFT) method.

gravity. The stretched adsorbent filament is about 600 μm wide. The NAF prepared by DIW has a flat surface and uniform morphology with a submillimeter scale three-dimensional grid structure formed by equally distributed adsorbent filaments. The macro channels of NAFs can increase the mass transfer area of pollutants and the fluid turbulivity compared to the PAFs. Thus, the inward diffusion and convective mass transfer of the VOCs will be enhanced [65].

3.2.2. *Adsorption behaviours of DIW fabricated adsorbent and raw material*

The pristine AC and ZSM-5 are shown in Fig. 3 (a) and (b). The particle size of activated carbon is uneven, with the smallest being less than 1 μm and the largest reaching 5 μm. ZSM-5 has long stripped particles with relatively uniform size, about 3–5 μm in length and 1–2 μm in width. Fig. 3 (c) and (d) respectively show the microscopic morphologies (magnification by 1000 times) of the material prepared by DIW before and after calcination. The morphology presented in Fig. 3 (d) looks fluffier and more porous than that in Fig. 3 (c). This phenomenon proved the amount of binder used for bonding between materials and plasticizer used for regulating rheological properties decreased after calcination. Thus, the blocked space is released, reducing the negative effect of binder and plasticizer on the adsorption properties of materials, which has been confirmed by previous studies [66,67]. It can be seen from the adsorption isotherms in Fig. 3 (e) – (h) that AC has the maximum adsorption capacity for N_2 under 70 K, about 530 $cm^3\ g^{-1}$ at standard temperature and pressure (STP), while ZSM-5, which is used to regulate AC rheological properties, has a weak adsorption capacity. As the mass ratio of AC and ZSM-5 in the DIW fabricated material is 1:2, the adsorption capacity of DIW fabricated material before calcination is proportional to the mass ratio of AC and ZSM-5, which is around 250 $cm^3\ g^{-1}$ STP. After annealing, the adsorption capacity increased by about 8% to 272 cm^3/g because of the carbonization of the organic binder and plasticizer during annealing, which may block the porous structure of the material. TGA results on the DIW fabricated material before and after annealing in Fig. S1 of Supplementary material showed that the mass decreases with the temperature for the adsorption film before annealing. There is a steep decrease at about 350 °C, which is the decomposition temperature for the additives. While for the annealed adsorption film, there is no apparent mass loss after annealing when the temperature comes to 200 °C and higher, proving the decomposition of the organic binder and plasticizer during annealing. In addition, when the relative pressure varies within the range of 0.4–1, the increase of N_2 adsorption capacity of the four materials is 8.0%, 6.4%, 11.8% and 12.9%, respectively. Since the increase of adsorption capacity under high pressure proved the existence of mesoporous (2–50 nm [68], defined by IUPAC), the difference in the shape of the adsorption isothermals explained the difference in pore size distribution: DIW preparation could generate additional mesopores, and calcination would further increase the content of mesopores. Fig. 3 (i) – (l) presented the SSA and DFT simulated by the DFT method. The pores of the four materials are mainly distributed within 4 nm. Compared with the material before and after calcination, the SSA increased by 4.5%. In particular, the BJH method calculated that the SSA generated by mesopore in the materials before and after calcination was 83 $m^2\ g^{-1}$ and

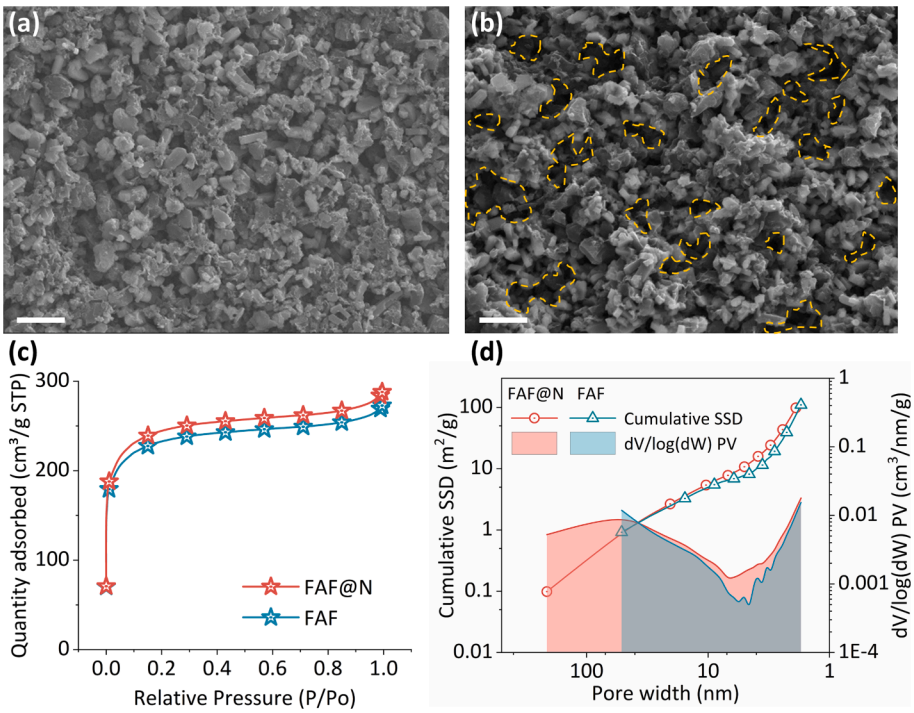

Fig. 4. The SEM images of the microscopic morphologies of the adsorption films (a) before (NAF) and (b) after (NAF@N) ammonia carbonate treatment, scale bars for (a) and (b), 10 μm. The orange dashed line described the additional micron-sized pores formed in the adsorption film after the ammonia carbonate treatment. (c) The adsorption isothermals of NAF@N and NAF. The static adsorption experiments are carried out with N_2 under 70 K. (d) The SSA and the PSD of NAF and NAF@N. The SSA and PSD are estimated using Barret Joyner Halenda (BJH) method, which can test pore size between 1.8 nm and 300 nm. The two adsorption films were both annealed. (For interpretation of the references to colour in this figure legend, the reader is referred to the web version of this article.)

110 m^2 g^{-1}, respectively, and the latter increased by about 33% compared with the former. It indicates that calcination can significantly improve the proportion of mesopores. Although the SSA cannot be greatly affected, the increase in the proportion of mesopores can promote the diffusion of gas molecules within the material, which significantly improves adsorption kinetics.

3.2.3. *The influences of ammonium carbonate treatment*

During the PAF@N and NAF@N fabrication process, the ammonium carbonate solution was dropwise added to the adsorption film. Ammonium carbonate acted as a pore-generation matter, which could decompose and produce ammonia gas and carbon dioxide by heating during the drying process, which would evaporate from the inside of the adsorption film through the material that had not yet dried. Because the adsorption film was still a water-containing viscous semi-solid at that time, a porous structure will be *in-situ* generated. Fig. 4 (a) and (b) respectively described the microscopic morphology of the adsorption films before (NAF) and after (NAF@N) ammonium carbonate treatment (both dried and annealed). Compared with NAF, the surface roughness of NAF@N increases, and there are many holes between 1 and 10 μm. When polluted air flows through adsorption film, the rise in roughness is conducive to improving airflow turbulence, strengthening the convective heat and mass transfer. It will benefit the dynamic adsorption performance and provoke heat and mass exchange during thermal regeneration. In addition, the formation of additional porous structures can provide channels for the inward diffusion of gaseous pollutants inside the adsorbent, thus increasing the diffusion flux. In addition, it can be seen from the adsorption isothermal in Fig. 4 (c) that the nitrogen adsorption capacity of NAF@N was enhanced from 273 cm^3 g^{-1} STP to 288 cm^3 g^{-1} compared with NAF when $P/P_0 = 1$. Besides, the SSAs of

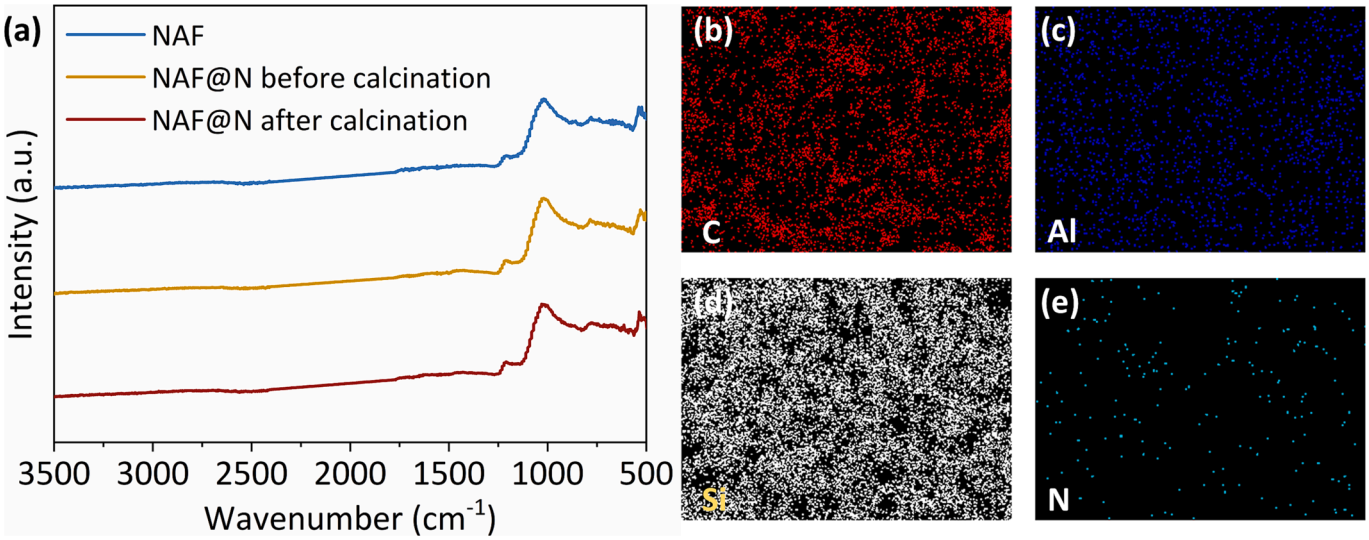

Fig. 5. (a) The FTIR spectrums of the NAF, the NAF@N before calcination and the NAF@N after calcination. The EDS images of NAF@N on (b) C element, (c) Al element, (d) Si element and (e) N element.

Formaldehyde	NAF@N	NAF	PAF@N	PAF
Performance decline	19.9%	25.6%	25.3%	36.6%
Purification rate (mg $g^{-1} h^{-1}$)	0.106	0.099	0.064	0.058

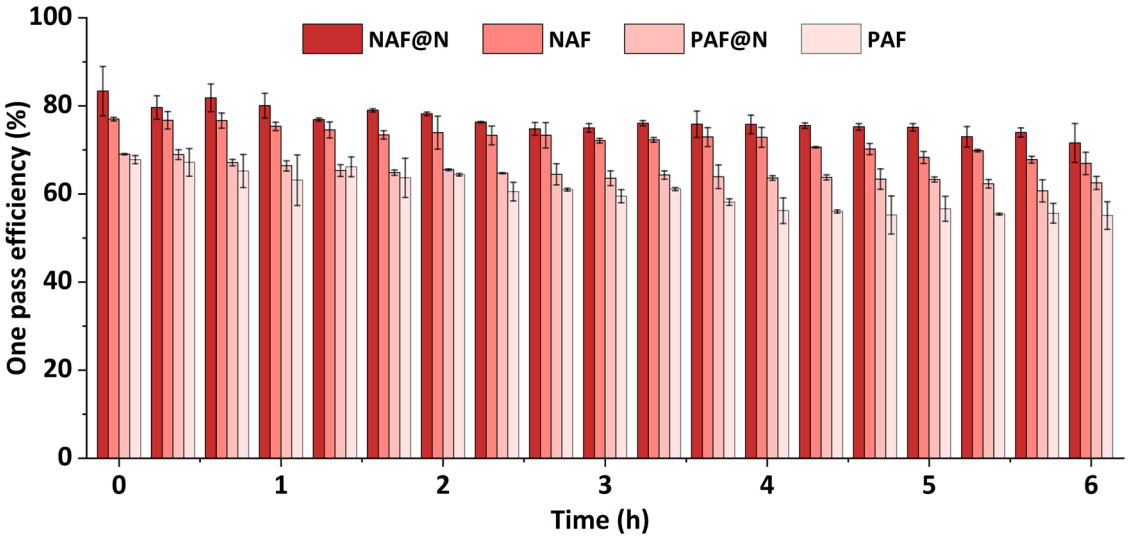

Fig. 6. One-pass efficiencies of NAF@N, NAF, PAF@N, and PAF during the formaldehyde dynamic adsorption process. The performance decline and the purification rate were calculated for each adsorption film listed in the attached table.

NAF and NAF@N simulated by the DFT method are 488 $m^2 g^{-1}$ and 496 $m^2 g^{-1}$, respectively. The latter only increased by 1.6%, but the SSAs of NAF and NAF@N induced by BJH mesopores were 110 $m^2 g^{-1}$ and 140 $m^2 g^{-1}$, respectively, enhanced by 27%. In the BJH mesoporous distribution diagram of Fig. 4 (d), the adsorption film after ammonium carbonate treatment has formed additional mesoporous in the range of 60–200 nm, indicating that the evaporation of ammonia and carbon dioxide promoted the formation of mesopores (2–50 nm) and macropores (greater than50 nm) and thus improved the mass transfer kinetics. The submicron-micron-sized pores induced by ammonium carbonate processing and DIW preparation provided hierarchical diffusion pathways for VOC molecules transport inside the adsorbent. Thus, the dynamic purification performance could be enhanced.

Fig. 5 (a) showed FTIR spectrums of the NAF, NAF@N before and after calcination. The results showed almost no difference in the infrared adsorption intensity. In particular, no additional amine group formation was detected near the wavenumber of 3000 cm^{-1}. In addition, the EDS diagram results from Fig. 5 (b) – (e) also show that the density of nitrogen is very small (maybe noise signal) compared with other elements, indicating that ammonium carbonate has been basically decomposed. Hence it can be concluded that the improvement of the adsorption performance of NAF@N relative to NAF is caused by physical factors (the formation of additional mesopores), which also means that such improvement of adsorption performance is applicable to the adsorption of various gas phase substances.

3.3. Dynamic adsorption behaviours for formaldehyde and toluene

Dynamic adsorption experiments of the four adsorption films (PAF, NAF, PAF@N, NAF@N) were conducted on an experimental setup [40]. The one-pass efficiency (ε) and purification rate (γ) were calculated to reflect their adsorption performances. The purification rate here means the adsorption amount per gram of adsorbent per hour during the dynamic adsorption process, which could be used to evaluate the adsorption rates of films. The one-pass efficiency is calculated by **Equation (1)**, and the purification rate is calculated by **Equation (2)**.

$$\varepsilon = \frac{C_{in} - C_{out}}{C_{in}} \tag{1}$$

$$\gamma = \frac{1}{t_e}\int_{t=0}^{t_e} \frac{G(C_{in} - C_{out})}{M} dt \tag{2}$$

where, ε is the one-pass efficiency; C_{in} is the inlet pollutant concentration, ppm; C_{out} is the outlet pollutant concentration, ppm; t_e is the experimental time, h; G is the polluted air flow rate, $m^3 s^{-1}$; M is the adsorbent mass, g.

3.3.1. The performance of four adsorption films on formaldehyde

Fig. 6 exhibits the adsorption performances of four adsorption films on formaldehyde, in which the inlet concentrations of formaldehyde are 2 mg m^{-3}. The initial one-pass efficiency of the PAF is about 67% for formaldehyde at the face velocity of 0.8 m s^{-1}, while the efficiency of the NAF is more than 75% with the same adsorbent thickness and face velocity. The one-pass efficiency declined slightly with time, to 57% after 6 h for NAF, and 44% for PAF. The purification rate was increased from 0.058 mg $g^{-1}h^{-1}$ for PAF to 0.099 mg $g^{-1}h^{-1}$ for NAF. As shown in Fig. 2 (e), inside the NAF, the pervasive macro channels induced by the DIW fabricated mutually perpendicular adsorbent filaments enable adequate contact between formaldehyde and adsorbent, and the uniformly distributed 0.6-mm wide adsorbent filaments extruded by DIW reduced the diffusion depth significantly compared with the PAF, whose thickness is 1.2 mm. In addition, when the pollutant flow passes through the NAF, the mutually perpendicular filaments generate more turbulence, enhancing the convection mass transfer.

As for PAF@N, the initial one-pass efficiency is around 69% percent for formaldehyde, nearly 3% higher than PAF, and the efficiency decreased to 52% after 6 h, as shown in Fig. 6. The purification rate of PAF@N was increased to 0.064 mg $g^{-1}h^{-1}$, 10% higher than the PAF. As shown in Fig. 4 (b), the submicron-micron-sized pores formed by ammonia gas and carbon dioxide evaporation created fast diffusion pathways for formaldehyde adsorption. Thus the mass transfer flux will be higher for PAF@N compared with PAF, inducing higher one-pass efficiency and greater purification rate.

Toluene	NAF@N	NAF	PAF@N	PAF
Performance decline	25.1%	28.3%	21.6%	26.6%
Purification rate(mg g^{-1} h^{-1})	0.239	0.227	0.154	0.143

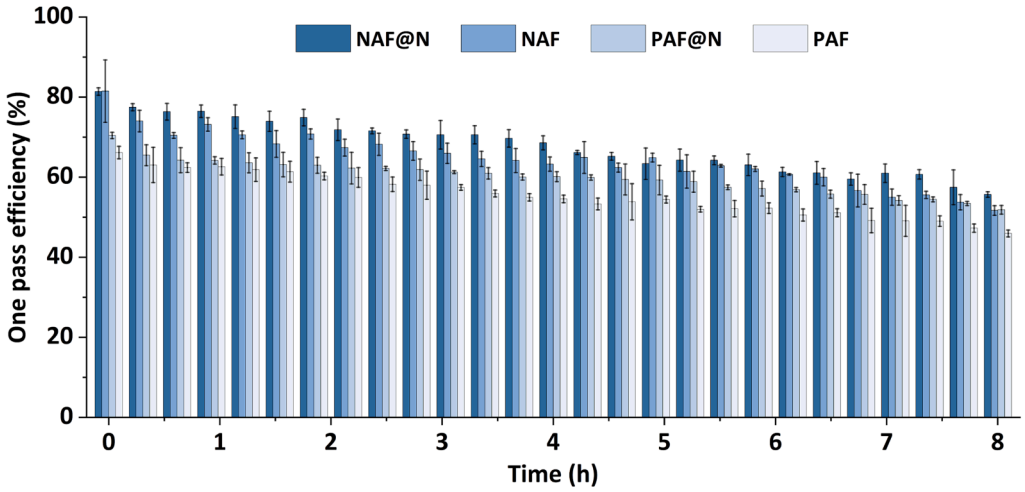

Fig. 7. One-pass efficiencies of NAF@N, NAF, PAF@N, and PAF during the toluene dynamic adsorption process. The performance decline and the purification rate were calculated for each adsorption film listed in the attached table.

For NAF@N, the formaldehyde adsorption performance is enhanced more significantly than NAF and PAF@N. As Fig. 6, The initial one-pass efficiency of NAF@N is about 81%, 6% higher than NAF, and the performance decline after 6 h is 19.9%, less than that of NAF and PAF@N, and the purification rate was 0.106 mg $g^{-1}h^{-1}$. The DIW fabrication created submillimeter-sized macro channels, reduced the diffusion depth and generated more turbulence; while the ammonium carbonate treatment induced submicron-micron-sized pores acting as fast diffusion pathways. The submicron-micron-submillimeter-sized hierarchical pathways enhanced both convective and diffusive mass transfer and significantly improved the formaldehyde removal performances.

3.3.2. *The performance of four adsorption films on toluene*

Fig. 7 exhibits the adsorption performances of four adsorption films on toluene, in which the inlet concentrations of toluene are 5 mg m^{-3}. Like formaldehyde, the NAF@N also presented the highest one-pass efficiency and purification rate for toluene, which are 82% and 0.239 mg $g^{-1}h^{-1}$, respectively, while the initial one-pass efficiencies of NAF, PAF@N and PAF are 82%, 70%, 66%, respectively.

During 8-hour experiments, the performance decline of each adsorption film for toluene did not exhibit the same tendency as that for formaldehyde. The performance decline of PAF in 8 h is 26.6% for toluene and 37.1% for formaldehyde in 6 h, indicating the pristine adsorbent has a better purification performance on toluene rather than formaldehyde. By ammonium carbonate treatment or DIW preparation, the toluene purification efficiency decline is generally reduced for PAF@N, NAF and NAF@N, but not as significant as formaldehyde. NAF performance decline was even more than PAF, which may be due to the large error at the first point of the NAF efficiency test, and the real efficiency may be lower than 82%. The enhancement of purification rate exhibited a similar tendency, that is, the purification rates of PAF@N, NAF and NAF@N for toluene increased by 8%, 59%, and 67%, respectively, while 10%, 71% and 83% for formaldehyde.

Generally, the performance improvement of toluene produced by DIW and ammonium carbonate treatment is less significant than that of formaldehyde. Compared with formaldehyde, toluene has a larger molecular weight and is more compatible with the physical and chemical structure of AC, so its distribution coefficient is higher than formaldehyde. Therefore, in the early adsorption process of toluene, the convection and surface distribution accounted for a larger proportion of the total adsorption mass transfer compared with formaldehyde, while the internal diffusion accounted for a relatively smaller proportion. However, according to the above analysis, the additional hierarchical pore structure in PAF@N, NAF and NAF@N mainly enhanced the diffusion of pollutants inward the adsorbent. Thus, the purification enhancement of PAF@N, NAF, and NAF@N is more significant for formaldehyde than toluene, which is also consistent with the previous study [63].

Table 1
The thermal regeneration ratio of adsorption films on formaldehyde and toluene after different regeneration times.

Regeneration time	Thermal regeneration ratio	
	Formaldehyde	Toluene
2 min	60.2%	53.9%
5 min	88.9%	76.2%
10 min	95.7%	85.0%
20 min	98.1%	92.1%
40 min	99.0%	97.8%
60 min		98.9%

Note: the adsorption films were heated at 80 °C for formaldehyde and 100 °C for toluene.

3.4. *Adsorption and regeneration cycles for formaldehyde and toluene*

Thermal regeneration was conducted to restore the performance of adsorption films. As NAF@N represented the best purifying performance, long-term dynamic adsorption-regeneration experiments were conducted on NAF@N for formaldehyde and toluene. One-pass efficiencies of NAF@N were monitored at the beginning of each cycle. The performance decline and regeneration ratios were calculated. The regeneration ratio is defined as **Equation (3)**.

$$rr^i = \frac{\varepsilon_r^i}{\varepsilon_a^i} \tag{3}$$

where, rr^i is the regeneration ratio for the i^{th} regeneration; i is equal to 1, 2 and 3, respectively; $\varepsilon_r{}^i$ is the initial one-pass removal efficiency after

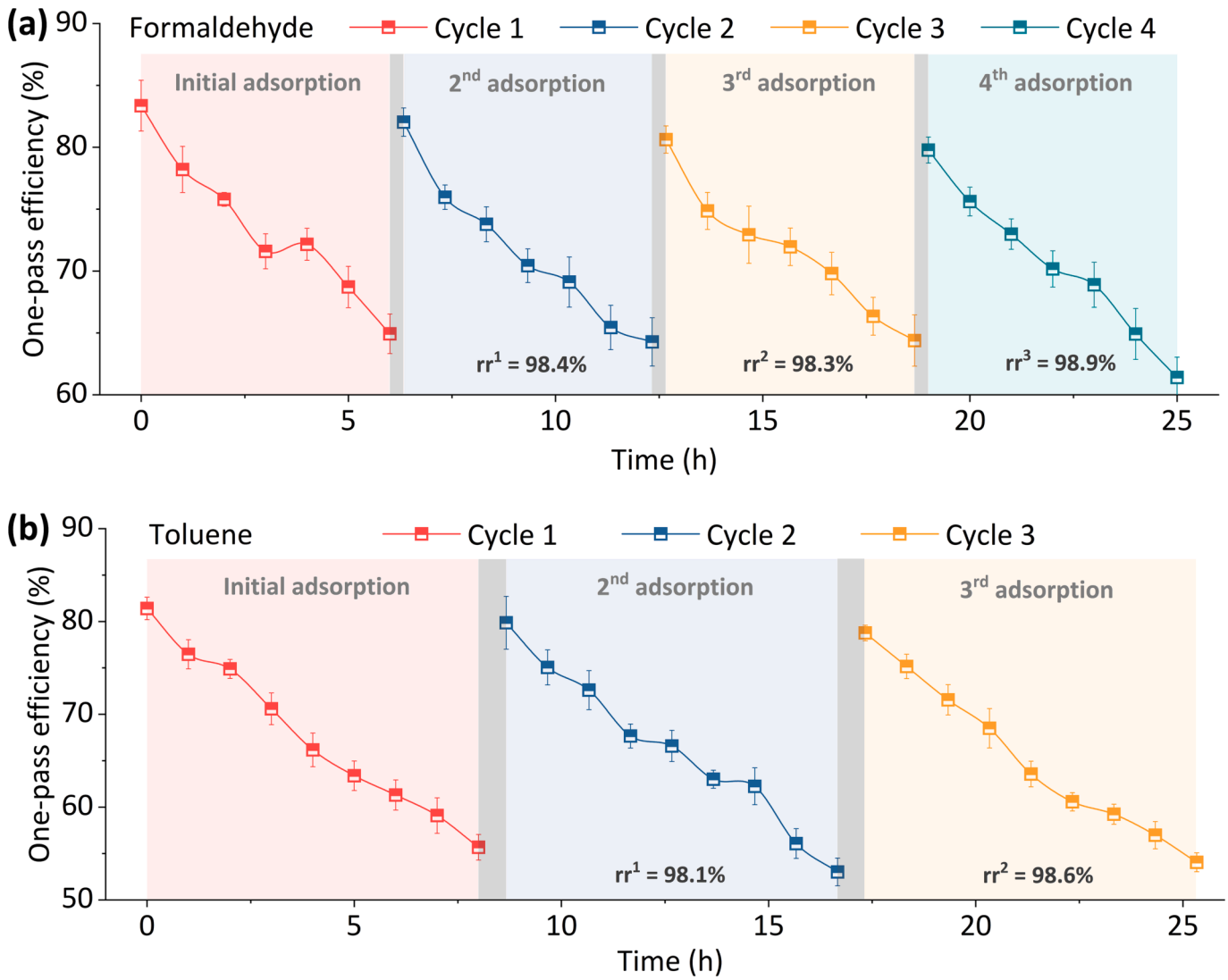

Fig. 8. Adsorption and regeneration cycles of NAF@N for (a) formaldehyde and (b) toluene for over 25 h. The grey blocks represent the thermal regeneration periods, which are 20 min for formaldehyde and 40 min for toluene. The regeneration ratios (*rr*) were calculated for each cycle based on Equation (3).

Table 2
The performance parameters of NAF@N for formaldehyde and toluene during the adsorption and regeneration cycles.

Regeneration cycle	Initial one-pass efficiency (%)	Performance decline (%)	Purification rate (mg $g^{-1}h^{-1}$))	Regeneration ratio (%)
	Formaldehyde			
Cycle 1	83.35	22.1	0.1056	–
Cycle 2	82.03	21.6	0.1026	98.4
Cycle 3	80.62	20.1	0.1025	98.3
Cycle 4	79.77	23.0	0.1016	98.9
	Toluene			
Cycle 1	81.40	31.6	0.2681	–
Cycle 2	79.86	31.9	0.2625	98.1
Cycle 3	78.76	31.4	0.2591	98.6

the i^{th} regeneration; and $\varepsilon_a{}^i$ is the initial one-pass removal efficiency before the i^{th} regeneration. The regeneration time for both formaldehyde and toluene was studied. Table 1 shows that the NAF@N is heated to 80 °C and 100 °C for formaldehyde and toluene desorption, respectively. After 2-min, 5-min, 10-min, 20-min and 40-min adsorption, the regeneration ratios are 60.2%, 88.9%, 95.7%, 98.1% and 99.0%. For long-term recycling, 20-min thermal desorption was finally chosen for formaldehyde adsorption-regeneration experiments. In comparison, the toluene desorption time was chosen as 40 min, with a regeneration ratio of 97.8%.

Over 24-hour experiments were conducted, in which 6-hour adsorption and 20-min regeneration for formaldehyde and 8-hour adsorption and 40-min regeneration for toluene. Fig. 8 and Table 2 showed that during 4 cycles, one-pass efficiencies of formaldehyde changed similarly. The performance declines are almost the same, with less than 5% variations. The purification rates of the 4 cycles are also nearly the same. The regeneration ratios all exceed 98%, indicating that 20-min regeneration can fully restore the adsorption performance of NAF@N. The performance changes and purification rates in the three cycles also remain the same for toluene. The regeneration ratios are 98.1% for cycle 2 and 98.6% for cycle 3, both of which reveal that 40-min regeneration is enough for toluene desorption.

XRD and XPS results of NAF@N before and after formaldehyde and toluene adsorption were shown in Fig. S2 and Fig. S3 of the Supplementary material. From XRD results, the three samples have similar peaks on each crystal face, which means the adsorption of formaldehyde or toluene will not change the crystal texture of the adsorbent. Subtle differences may result from the different locations of the selected

Table 3
Recent studies on the adsorption component fabrication for indoor gas adsorption.

Adsorbents	Structures	Preparation method	Target gas	Face velocity (m/s)	Initial efficiency	Break-through time (h)	Ref.
Cu-CPP/Al_2O_3	packed bed	–	Toluene	0.005	100%	13.3	[69]
Al_2O_3	packed bed	–	Toluene	0.005	90%	1.5	[69]
AC	packed bed	–	Toluene	0.005	82%	9.7	[69]
AC	packed bed	–	Toluene	0.002	100%	20	[70]
CTF-1–400	packed bed	–	Toluene	0.002	100%	27	[70]
ClCTF-1–400	packed bed	–	Toluene	0.002	100%	46	[70]
PDMS@MIL-125-R7	Fibre adsorber	–	Toluene	0.005	62%	0.42	[71]
PDMS@MIL-125-NH2	Fibre adsorber	–	Toluene	0.005	82%	0.75	[71]
AC/ACF	Fibre adsorber	–	Toluene	–	100%	0.21	[72]
AC/ACF	Fibre adsorber	–	n-Butane	–	100%	0.03	[72]
mordenite	packed bed	–	Benzene	0.02	100%	0.21	[73]
β zeolites	packed bed	–	Benzene	0.02	100%	0.38	[73]
AC	Adsorption film	DIW	Xylene	0.8	70%	30	[64]
AC	Adsorption film	DIW	Formaldehyde	0.8	65%	3.8	[64]
AC	Adsorption film	DIW	Xylene	0.8	45%	75	[63]
AC	Adsorption film	DIW	Formaldehyde	0.8	43%	6	[63]
AC	packed bed	–	Toluene	20 mL/min	100%	1	[74]
AC@CuO	packed bed	–	Toluene	20 mL/min	100%	1.8	[74]
HKUST-1	packed bed	–	Formaldehyde	400 mL/min	100%	8.3	[75]
ZSM-5/silica	monolith	DIW	Toluene	–	100%	0.19	[43]
AC	packed bed	–	Butane	0.05	100%	0.23	[44]
AC	monolith	DLP	Butane	0.05	100%	0.55	[44]
AC	microchannel monolith	DLP	Butane	0.05	100%	0.63	[44]
PIM-1	Fibre adsorber	–	Toluene	0.005	100%	0.42	[47]
PIM-1	packed bed	–	Toluene	0.005	100%	2.22	[47]
PIM-1	monolith	DIW	Toluene	0.005	100%	5.56	[47]
ABS	monolith	FDM	DMMP	0.04	95%	1.33	[76]
ABS/ZnO	monolith	FDM	DMMP	0.04	96%	1.67	[76]
ABS/ZIF-8	monolith	FDM	DMMP	0.04	98%	1.83	[76]
ZSM-5	adsorption film	DIW	Formaldehyde	0.8	40%	0.82	[40]
ZSM-5	finned adsorption film	DIW	Formaldehyde	0.8	57%	1.76	[40]
ZSM-5	double-layer finned film	DIW	Formaldehyde	0.8	58%	2.77	[40]
Y/ZSM-5 zeolite	packed bed	–	Toluene	0.06	100%	0.72	[77]
Y/ZSM-5 zeolite	packed bed	–	Cyclohexane	0.06	100%	0.33	[77]
Y/ZSM-5 zeolite	packed bed	–	Butyl acetate	0.06	100%	1.6	[77]
Y/ZSM-5 zeolite	packed bed	–	Isopropanol	0.06	100%	0.87	[77]
Na-MOR zeolite	monolith	molding	toluene	0.003	100%	0.23	[78]
ZSM-5 zeolites	monolith	DIW	methane	0.01	100%	0.08	[20]
ZIF-8 zeolites	monolith	DIW	n-butanol	0.005	100%	48	[79]
ZIF-8 zeolites	monolith	DIW	n-butanol	0.005	100%	27	[80]
SAPO-34 zeolites	monolith	DIW	CO_2	0.002	100%	0.04	[81]
NaY zeolites	monolith	molding	CO_2	0.02	100%	0.28	[82]
zeolite 13X/5A	monolith	DIW	CO_2	0.004	100%	0.16	[29]
NaX zeolite	monolith	DIW	CO_2	–	100%	1.03	[30]
zeolite 13X	monolith	DIW	CO_2	0.005	100%	1	[21]
clay	monolith	DIW	xylene	100 mL/min	100%	1.1	[83]
AC/ZSM-5@N	net-like adsorption film	DIW	Formaldehyde	0.8	82%	Over 12 (Exp)	This study
AC/ZSM-5@N	net-like adsorption film	DIW	Toluene	0.8	81%	Over 16 (Exp)	This study

Notes: Cu-CPP is short for copper coordination polymer particles, CTF is short for Covalent triazine framework, PIM-1 is a microporous polymer, and DMMP is short for dimethyl methyl phosphonate. "-" means the data is not given in the research article. DLP is short for digital light processing, FDM is short for fused deposition modelling. "Exp" means the data is expected based on the experimental results.

material and differences in the crystallinity and particle size of different regions of the material. Furthermore, from the XPS results, it can be seen that there are no significant differences no matter in the valence states of the various elements in these materials, the type and amount of chemical bonds, or the bond energy. In conclusion, no significant chemical structure changes were detected before and after the adsorption of formaldehyde and toluene, which means the adsorption of formaldehyde or toluene in this study should be physical sorption. The adsorption process is reversible, and the hierarchical porous adsorption films are stable. The adsorption-regeneration cycles also evidenced this inference. The adsorption performance can be generally restored after thermal regeneration from Fig. 8.

In conclusion, the chemical structures of NAF@N are stable during the adsorption of formaldehyde and toluene, and it can be almost fully regenerated by one-hour heating at 80 °C for formaldehyde and 100 °C for toluene, showing a promising long-term pollutants removal capability for clean indoor environment.

3.5. Performance comparisons with 3D printed adsorbents in other studies

Recent studies on the adsorption component fabrication for indoor gas adsorption, especially VOC adsorptive removal, have been reviewed comprehensively, including activated carbon, ceramic adsorbent, MOF and polymer adsorbent. The material compositions, structure types, preparation methods, and breakthrough curve parameters reflecting their dynamic adsorption capacity are listed in Table 3 below, including the initial one-pass efficiency and breakthrough time (defined as the time when the one-pass efficiency decreased to half of the initial one-pass efficiency). The performances of NAF@N proposed in this study are also attached here. From the table, activated carbon materials are most commonly used in indoor VOC purification, followed by ceramic adsorbents (zeolites), because they are cheap, easily accessible, and have well-developed porous structures. The ceramic adsorbents are not only used for VOC removal, but also applicable for CO_2 capture and separation. The structures of adsorption components can be divided into four types: packed bed, fibre adsorber, adsorption monolith and adsorption film. The latter two are structured adsorption components, which can be prepared by extrusion molding, DLP (digital light processing), FDM (fused deposition modeling) and DIW method. From Ref. [44], the breakthrough time of the adsorption monolith is about 3 times as long as that of the packed bed under the same conditions. Ref. [47] also shows that the breakthrough time of the adsorption monolith is 2.5 times as long as that of the packed bed and more than 10 times larger than the fibre adsorber with the same experimental parameters. In most of these studies, the face velocities are controlled very low, only $10^{-3} - 10^{-2}$ m/s, so the initial one-pass efficiency could reach 100%. The breakthrough time, however, is relatively short, within 10 h for most of the studies, some even within 1 h for most of the adsorption components in these studies, which is unsuitable for practical applications. The adsorption component of Ref. [63,64] can maintain a long life for xylene removal at 0.8 m/s, but its initial efficiency is not high enough. The NAF@N proposed in this paper can achieve 82% and 81% efficiency of formaldehyde and toluene, respectively, at 0.8 m/s. During the 6 h and 8 h breakthrough experiments for formaldehyde and toluene, respectively, the performance declines are less than 30% for both formaldehyde and toluene. The breakthrough time of NAF@N is estimated to be more than 12 h and more than 16 h for formaldehyde and toluene, respectively. By constructing perpendicular filaments of material on the surface of the adsorption film through DIW, the submillimeter-sized macro channels were created, reducing the diffusion depth, promoting pollutants moving into the material, and generating more turbulence for convective mass transfer. While the ammonium carbonate treatment induced submicron-micron-sized pores, which acted as fast diffusion pathways for pollutant molecules to diffuse inside the adsorbent. The submicron-micron-submillimeter-sized hierarchical pathways enhanced both convective and diffusive mass transfer and significantly improved the formaldehyde and toluene removal performances. The temperature-controllable substrate of NAF@N can recover the performance of over 95% within a short time (20 min for formaldehyde, 40 min for toluene) by *in-situ* electric heating. Compared with other studies, NAF@N can fully meet the purification requirements in practical applications and can be used for long-term control of indoor gaseous pollutants.

4. Conclusions

This study proposed a fabrication method for hierarchical diffusion pathways into VOC adsorption films by direct ink writing and ammonium carbonate treatment. The results of SEM images, adsorption isothermals, and pore size distribution showed that the submicron-micron-submillimeter-sized porous adsorption films were fabricated (NAF@N). From dynamic adsorption and regeneration experiments on formaldehyde and toluene, the NAF@N processed by both DIW and ammonium carbonate treatment has the best adsorption performance. The NAF@N exhibited an over 80% initial one-pass efficiency for both formaldehyde and toluene, which is improved by around 20% over the NAF. The purification rate was also significantly improved by 83% and 67% for formaldehyde and toluene. After 6-hour adsorption of formaldehyde and 8-hour adsorption of toluene, the performances decreased by 22.1% and 25.1% for formaldehyde and toluene and were restored through 20 min heating at 80 °C and 40 min heating at 100 °C, respectively. The DIW-induced sub-millimetre-sized channels and the gas evaporation-induced submicron-micron-sized pores contribute to the formation of submicron-micron-submillimetre-sized hierarchical gas diffusion pathways. Thus the gaseous pollutants could rapidly diffuse into the adsorbent and exhibit a high one-pass efficiency and a great purification rate, leading to the brilliant adsorption behaviours of the NAF@N. This DIW method with ammonium carbonate treatment offers additional potential for fabricating adsorption films with hierarchical porous structures to meet practical needs for various applications, including indoor air purification, carbon capture and storage and gas separation in chemical engineering.

Declaration of Competing Interest

The authors declare that they have no known competing financial interests or personal relationships that could have appeared to influence the work reported in this paper.

Data availability

Data will be made available on request.

Acknowledgements

This work was financially supported by the National Natural Science Foundation of China (No. 52078269).

Appendix A. Supplementary data Thermogravimetric analysis on the adsorption film before and after annealing (Fig. S1). The XRD results of the NAF@N before and after formaldehyde and toluene adsorption. (Fig. S2). The XPS results of the NAF@N before and after formaldehyde and toluene adsorption (Fig. S3).

Supplementary data to this article can be found online at https://doi.org/10.1016/j.cej.2023.144560.

References

[1] D.E. Hun, R.L. Corsi, M.T. Morandi, J.A. Siegel, Formaldehyde in residences: long-term indoor concentrations and influencing factors, Indoor Air 20 (3) (2010) 196–203, https://doi.org/10.1111/j.0905-6947.2010.00644.x.

[2] Y. Wang, H. Wang, Y. Tan, J. Liu, K. Wang, W. Ji, L. Sun, X. Yu, J. Zhao, B. Xu, J. Xiong, Measurement of the key parameters of VOC emissions from wooden furniture, and the impact of temperature, Atmos. Environ. 259 (2021), 118510, https://doi.org/10.1016/j.atmosenv.2021.118510.

[3] Z. Chen, Q. Chen, Y. Xu, J. Mo, Partitioning characteristics of indoor VOCs on impermeable surfaces covered by film-phase DnBP and DEHP, J. Hazard. Mater. Adv. 8 (2022) 100191.

[4] X. Zhou, Z. Gao, X. Wang, F. Wang, Mathematical model for characterizing the full process of volatile organic compound emissions from paint film coating on porous substrates, Build. Environ. 182 (2020), 107062, https://doi.org/10.1016/j.buildenv.2020.107062.

[5] A. Bradman, F. Gaspar, R. Castorina, J. Williams, T. Hoang, P.L. Jenkins, T. E. McKone, R. Maddalena, Formaldehyde and acetaldehyde exposure and risk characterization in California early childhood education environments, Indoor Air 27 (1) (2017) 104–113, https://doi.org/10.1111/ina.12283.

[6] Z. Du, J. Mo, Y. Zhang, Risk assessment of population inhalation exposure to volatile organic compounds and carbonyls in urban China, Environ. Int. 73 (2014) 33–45, https://doi.org/10.1016/j.envint.2014.06.014.

[7] Z. Chen, Q. Wu, Y. Xu, J. Mo, Partitioning of airborne PAEs on indoor impermeable surfaces: a microscopic view of the sorption process, J. Hazard. Mater. 424 (Pt A) (2022), 127326, https://doi.org/10.1016/j.jhazmat.2021.127326.

[8] Y. Gao, E. Tian, J. Mo, Electrostatic Polydopamine-Interface-Mediated (e-PIM) filters with tuned surface topography and electrical properties for efficient particle capture and ozone removal, J. Hazard. Mater. 441 (2023), 129821, https://doi.org/10.1016/j.jhazmat.2022.129821.

[9] Y. Zhang, J. Mo, Y. Li, J. Sundell, P. Wargocki, J. Zhang, J.C. Little, R. Corsi, Q. Deng, M.H.K. Leung, L. Fang, W. Chen, J. Li, Y. Sun, Can commonly-used fan-driven air cleaning technologies improve indoor air quality? A literature review, Atmos. Environ. 45 (26) (2011) 4329–4343, https://doi.org/10.1016/j.atmosenv.2011.05.041.

[10] X. Zhang, B. Gao, A.E. Creamer, C. Cao, Y. Li, Adsorption of VOCs onto engineered carbon materials: a review, J. Hazard. Mater. 338 (2017) 102–123, https://doi.org/10.1016/j.jhazmat.2017.05.013.

[11] A. Luengas, A. Barona, C. Hort, G. Gallastegui, V. Platel, A. Elias, A review of indoor air treatment technologies, Rev. Environ. Sci. Biotechnol. 14 (3) (2015) 499–522, https://doi.org/10.1007/s11157-015-9363-9.

[12] R.R. Gil, B. Ruiz, M.S. Lozano, M.J. Martín, E. Fuente, VOCs removal by adsorption onto activated carbons from biocollagenic wastes of vegetable tanning, Chem. Eng. J. 245 (2014) 80–88, https://doi.org/10.1016/j.cej.2014.02.012.

[13] J. Jeon, J.H. Park, S. Wi, B.Y. Yun, T. Kim, S. Kim, Field study on the improvement of indoor air quality with toluene adsorption finishing materials in an urban residential apartment, Environ. Pollut. 261 (2020), 114137, https://doi.org/10.1016/j.envpol.2020.114137.

[14] M.E.E. Abashar, A.A. Al-Rabiah, Highly efficient CO2 hydrogenation to methanol via in-situ condensation and sorption in a novel multi-stage circulating fast fluidized bed reactor, Chem. Eng. J. 439 (2022) 135628.

[15] S. Nilsson, A. Ronda, A. Gómez-Barea, Kinetics of H2S removal using alkaline residue as in-bed sorbent in fluidized bed gasification of biomass and wastes, Chem. Eng. J. 464 (2023) 142460.

[16] Y. Wang, T. Yu, J. Mo, The influence of indoor environmental factors on toluene uptake rate of a tube-type diffusive sampler, J. Build. Eng. 54 (2022) 104587.

[17] Y. Wang, T. Yu, J. Mo, Prediction and validation of diffusive uptake rates for indoor volatile organic compounds in axial passive samplers, Energy Built Environ. (2022), https://doi.org/10.1016/j.enbenv.2022.07.004.

[18] G. Moussavi, R. Rashidi, A. Khavanin, The efficacy of GAC/MgO composite for destructive adsorption of benzene from waste air stream, Chem. Eng. J. 228 (2013) 741–747, https://doi.org/10.1016/j.cej.2013.05.032.

[19] H.-B. Liu, B. Yang, N.-D. Xue, Enhanced adsorption of benzene vapor on granular activated carbon under humid conditions due to shifts in hydrophobicity and total micropore volume, J. Hazard. Mater. 318 (2016) 425–432, https://doi.org/10.1016/j.jhazmat.2016.07.026.

[20] S. Couck, J. Lefevere, S. Mullens, L. Protasova, V. Meynen, G. Desmet, G.V. Baron, J.F.M. Denayer, CO2, CH4 and N2 separation with a 3DFD-printed ZSM-5 monolith, Chem. Eng. J. 308 (2017) 719–726, https://doi.org/10.1016/j.cej.2016.09.046.

[21] S. Lawson, B. Adebayo, C. Robinson, Q. Al-Naddaf, A.A. Rownaghi, F. Rezaei, The effects of cell density and intrinsic porosity on structural properties and adsorption kinetics in 3D-printed zeolite monoliths, Chem. Eng. Sci. 218 (2020), 115564, https://doi.org/10.1016/j.ces.2020.115564.

[22] J. Zhu, P. Wu, Y. Chao, J. Yu, W. Zhu, Z. Liu, C. Xu, Recent advances in 3D printing for catalytic applications, Chem. Eng. J. 433 (2022), 134341, https://doi.org/10.1016/j.cej.2021.134341.

[23] E.R. Kearns, R. Gillespie, D.M. D'Alessandro, 3D printing of metal–organic framework composite materials for clean energy and environmental applications, J. Mater. Chem. A 9 (48) (2021) 27252–27270, https://doi.org/10.1039/d1ta08777k.

[24] F.A. Hasan, P. Xiao, R.K. Singh, P.A. Webley, Zeolite monoliths with hierarchical designed pore network structure: Synthesis and performance, Chem. Eng. J. 223 (2013) 48–58, https://doi.org/10.1016/j.cej.2013.02.100.

[25] F. Rezaei, P. Webley, Structured adsorbents in gas separation processes, Sep. Purif. Technol. 70 (3) (2010) 243–256, https://doi.org/10.1016/j.seppur.2009.10.004.

[26] W.Y. Hong, S.P. Perera, A.D. Burrows, Manufacturing of metal-organic framework monoliths and their application in CO 2 adsorption, Microporous Mesoporous Mater. 214 (2015) 149–155, https://doi.org/10.1016/j.micromeso.2015.05.014.

[27] A. Pereira, A.F.P. Ferreira, A. Rodrigues, A.M. Ribeiro, M.J. Regufe, Shaping of ZIF-8 and MIL-53(Al) adsorbents for CH4/N2 separation, Microporous Mesoporous Mater. 331 (2022), 111648, https://doi.org/10.1016/j.micromeso.2021.111648.

[28] S. Lawson, A.-A. Alwakwak, A.A. Rownaghi, F. Rezaei, Gel–print–grow: A new way of 3D printing metal–organic frameworks, ACS Appl. Mater. Interfaces 12 (50) (2020) 56108–56117, https://doi.org/10.1021/acsami.0c18720.

[29] H. Thakkar, S. Lawson, A.A. Rownaghi, F. Rezaei, Development of 3D-printed polymer-zeolite composite monoliths for gas separation, Chem. Eng. J. 348 (2018) 109–116, https://doi.org/10.1016/j.cej.2018.04.178.

[30] S. Wang, P. Bai, M. Sun, W. Liu, D. Li, W. Wu, W. Yan, J. Shang, J. Yu, Fabricating mechanically robust binder-free structured zeolites by 3D printing coupled with zeolite soldering: A superior configuration for CO2 capture, Adv. Sci. 6 (17) (2019) 1901317, https://doi.org/10.1002/advs.201901317.

[31] C. Zhu, Z. Qi, V.A. Beck, M. Luneau, J. Lattimer, W. Chen, M.A. Worsley, J. Ye, E. B. Duoss, C.M. Spadaccini, C.M. Friend, J. Biener, Toward digitally controlled catalyst architectures: Hierarchical nanoporous gold via 3D printing, Sci. Adv. 4 (8) (2018), https://doi.org/10.1126/sciadv.aas9459.

[32] Z. Chen, Z. Li, J. Li, C. Liu, C. Lao, Y. Fu, C. Liu, Y. Li, P. Wang, Y. He, 3D printing of ceramics: A review, J. Eur. Ceram. Soc. 39 (4) (2019) 661–687, https://doi.org/10.1016/j.jeurceramsoc.2018.11.013.

[33] A. Corker, H.C. Ng, R.J. Poole, E. Garcia-Tunon, 3D printing with 2D colloids: designing rheology protocols to predict 'printability' of soft-materials, Soft Matter 15 (6) (2019) 1444–1456, https://doi.org/10.1039/c8sm01936c.

[34] L. Hao, D. Tang, T. Sun, W. Xiong, Z. Feng, K.E. Evans, Y. Li, Direct ink writing of mineral materials: a review, Int. J. Precis. Eng. Manuf. Green Technol. 8 (2) (2020) 665–685, https://doi.org/10.1007/s40684-020-00222-6.

[35] Q. Chen, E. Tian, Y. Wang, J. Mo, G. Xu, M. Zhu, Recent progress and perspectives of direct ink writing applications for mass transfer enhancement in gas-phase adsorption and catalysis, Small Methods (2023) e2201302.

[36] X. Zhou, C.-J. Liu, Three-dimensional printing for catalytic applications: Current status and perspectives, Adv. Funct. Mater. 27 (30) (2017) 1701134, https://doi.org/10.1002/adfm.201701134.

[37] H.A. Loh, A.R. Graves, C.D. Stinespring, K.A. Sierros, Direct ink writing of graphene-based solutions for gas sensing, ACS Appl. Nano Mater. 2 (7) (2019) 4104–4112, https://doi.org/10.1021/acsanm.9b00572.

[38] C.A. Grande, R. Blom, V. Middelkoop, D. Matras, A. Vamvakeros, S.D.M. Jacques, A.M. Beale, M. Di Michiel, K. Anne Andreassen, A.M. Bouzga, Multiscale investigation of adsorption properties of novel 3D printed UTSA-16 structures, Chem. Eng. J. 402 (2020), 126166, https://doi.org/10.1016/j.cej.2020.126166.

[39] V. Middelkoop, K. Coenen, J. Schalck, M. Van Sint Annaland, F. Gallucci, 3D printed versus spherical adsorbents for gas sweetening, Chem. Eng. J. 357 (2019) 309–319, https://doi.org/10.1016/j.cej.2018.09.130.

[40] Q. Chen, E. Tian, Z. Luo, J. Mo, Adsorption film with sub-milli-interface morphologies via direct ink writing for indoor formaldehyde removal, J. Hazard. Mater. 427 (2022), 128190, https://doi.org/10.1016/j.jhazmat.2021.128190.

[41] T. Li, J. Gonzalez-Gutierrez, I. Raguž, C. Holzer, M. Li, P. Cheng, M. Kitzmantel, L. Shi, L. Huang, Material extrusion additively manufactured alumina monolithic structures to improve the efficiency of plasma-catalytic oxidation of toluene, Addit. Manuf. 37 (2021), 105546, https://doi.org/10.1016/j.addma.2020.101700.

[42] Y. Pan, P. Zhu, R. Wang, Z. Si, B. Li, Y. Yao, Direct ink writing of porous cordierite honeycomb ceramic, Ceram. Int. 45 (12) (2019) 15230–15236, https://doi.org/10.1016/j.ceramint.2019.05.011.

[43] S. Wang, P. Bai, Y. Wei, W. Liu, X. Ren, J. Bai, Z. Lu, W. Yan, J. Yu, Three-dimensional-printed core-shell structured MFI-type zeolite monoliths for volatile organic compound capture under humid conditions, ACS Appl. Mater. Interfaces 11 (42) (2019) 38955–38963, https://doi.org/10.1021/acsami.9b13819.

[44] S. Scott, J. Chew, J. Barnard, A. Burrows, M. Smith, S. Tennison, S. Perera, Tailoring 3D Printed Micro-Structured Carbons for Adsorption, Adv. Funct. Mater. (2023), https://doi.org/10.1002/adfm.202213715.

[45] S. Zhao, G. Siqueira, S. Drdova, D. Norris, C. Ubert, A. Bonnin, S. Galmarini, M. Ganobjak, Z. Pan, S. Brunner, G. Nystrom, J. Wang, M.M. Koebel, W.J. Malfait, Additive manufacturing of silica aerogels, Nature 584 (7821) (2020) 387–392, https://doi.org/10.1038/s41586-020-2594-0.

[46] S. Lawson, A. Farsad, F. Rezaei, D. Ludlow, A.A. Rownaghi, Direct ink writing of metal oxide/H-ZSM-5 catalysts for n-Hexane cracking: a new method of additive manufacturing with high metal oxide loading, ACS Appl. Mater. Interfaces 13 (1) (2021) 781–794, https://doi.org/10.1021/acsami.0c20752.

[47] F. Zhang, Y. Ma, J. Liao, V. Breedveld, R.P. Lively, Solution-based 3D printing of polymers of intrinsic microporosity, Macromol. Rapid Commun. 39 (13) (2018) e1800274.

[48] M. Ouzzine, A.J. Romero-Anaya, M.A. Lillo-Ródenas, A. Linares-Solano, Spherical activated carbons for the adsorption of a real multicomponent VOC mixture, Carbon 148 (2019) 214–223, https://doi.org/10.1016/j.carbon.2019.03.075.

[49] M.J. Regufe, A.F.P. Ferreira, J.M. Loureiro, A. Rodrigues, A.M. Ribeiro, Electrical conductive 3D-printed monolith adsorbent for CO2 capture, Microporous Mesoporous Mater. 278 (2019) 403–413, https://doi.org/10.1016/j.micromeso.2019.01.009.

[50] J. Luo, B. Liu, R. Shi, Y. Guo, Q. Feng, Z. Liu, L. Li, K. Norinaga, The effects of nitrogen functional groups and narrow micropore sizes on CO2 adsorption onto N-doped biomass-based porous carbon under different pressure, Microporous Mesoporous Mater. 327 (2021), 111404, https://doi.org/10.1016/j.micromeso.2021.111404.

[51] H. Wang, R. Zhang, D. Yuan, S. Xu, L. Wang, Gas foaming guided fabrication of 3D porous plasmonic nanoplatform with broadband absorption, tunable shape, excellent stability, and high photothermal efficiency for solar water purification,

Adv. Funct. Mater. 30 (46) (2020) 2003995, https://doi.org/10.1002/adfm.202003995.
[52] L. Alison, S. Menasce, F. Bouville, E. Tervoort, I. Mattich, A. Ofner, A.R. Studart, 3D printing of sacrificial templates into hierarchical porous materials, Sci. Rep. 9 (1) (2019) 409, https://doi.org/10.1038/s41598-018-36789-z.
[53] A. Davó-Quiñonero, D. Sorolla-Rosario, E. Bailón-García, D. Lozano-Castelló, A. Bueno-López, Improved asymmetrical honeycomb monolith catalyst prepared using a 3D printed template, J. Hazard. Mater. 368 (2019) 638–643, https://doi.org/10.1016/j.jhazmat.2019.01.092.
[54] M.R. Sommer, M. Schaffner, D. Carnelli, A.R. Studart, 3D Printing of hierarchical silk fibroin structures, ACS Appl. Mater. Interfaces 8 (50) (2016) 34677–34685, https://doi.org/10.1021/acsami.6b11440.
[55] S. Lawson, K. Newport, Q. Al-Naddaf, A.E. Ameh, A.A. Rownaghi, L.F. Petrik, F. Rezaei, Binderless zeolite monoliths production with sacrificial biopolymers, Chem. Eng. J. 407 (2021), 128011, https://doi.org/10.1016/j.cej.2020.128011.
[56] W.-Y. Yan, C. Zhang, L. Liu, Hierarchically Porous CuAg via 3D Printing/Dealloying for Tunable CO2 Reduction to Syngas, ACS Appl. Mater. Interfaces 13 (38) (2021) 45385–45393, https://doi.org/10.1021/acsami.1c10564.
[57] J. Zhao, G. Luo, J. Wu, H. Xia, Preparation of microporous silicone rubber membrane with tunable pore size via solvent evaporation-induced phase separation, ACS Appl. Mater. Interfaces 5 (6) (2013) 2040–2046, https://doi.org/10.1021/am302929c.
[58] Q. Liu, W. Zhai, Hierarchical Porous Ceramics with Distinctive Microstructures by Emulsion-Based Direct Ink Writing, ACS Appl. Mater. Interfaces 14 (28) (2022) 32196–32205, https://doi.org/10.1021/acsami.2c03245.
[59] K. Huang, H. Elsayed, G. Franchin, P. Colombo, 3D printing of polymer-derived SiOC with hierarchical and tunable porosity, Addit. Manuf. 36 (2020), 101549, https://doi.org/10.1016/j.addma.2020.101549.
[60] D. Liu, P. Jiang, X. Li, J. Liu, L. Zhou, X. Wang, F. Zhou, 3D printing of metal-organic frameworks decorated hierarchical porous ceramics for high-efficiency catalytic degradation, Chem. Eng. J. 397 (2020), 125392, https://doi.org/10.1016/j.cej.2020.125392.
[61] M.A. Sidheswaran, H. Destaillats, D.P. Sullivan, S. Cohn, W.J. Fisk, Energy efficient indoor VOC air cleaning with activated carbon fiber (ACF) filters, Build. Environ. 47 (2012) 357–367, https://doi.org/10.1016/j.buildenv.2011.07.002.
[62] H. Chen, J. Mo, R. Xiao, E. Tian, Gaseous formaldehyde removal: A laminated plate fabricated with activated carbon, polyimide, and copper foil with adjustable surface temperature and capable of in situ thermal regeneration, Indoor Air 29 (3) (2019) 469–476, https://doi.org/10.1111/ina.12540.
[63] Q. Chen, F. Liu, J. Mo, Vertical macro-channel modification of a flexible adsorption board with in-situ thermal regeneration for indoor gas purification to increase effective adsorption capacity, Environ. Res. 192 (2021), 110218, https://doi.org/10.1016/j.envres.2020.110218.
[64] Q. Chen, R. Xiao, X. Lei, T. Yu, J. Mo, Experimental and modeling investigations on the adsorption behaviors of indoor volatile organic compounds in an in-situ thermally regenerated adsorption-board module, Build. Environ. 203 (2021), 108065, https://doi.org/10.1016/j.buildenv.2021.108065.
[65] In Seok Kang, Ho Nam Chang, The effect of turbulence promoters on mass transfer—numerical analysis and flow visualization, Int. J. Heat Mass Transf. 25 (8) (1982) 1167–1181.
[66] H. Thakkar, S. Eastman, A. Hajari, A.A. Rownaghi, J.C. Knox, F. Rezaei, 3D-printed zeolite monoliths for CO2 removal from enclosed environments, ACS Appl. Mater. Interfaces 8 (41) (2016) 27753–27761, https://doi.org/10.1021/acsami.6b16732.
[67] H. Thakkar, S. Eastman, A. Al-Mamoori, A. Hajari, A.A. Rownaghi, F. Rezaei, Formulation of aminosilica adsorbents into 3D-Printed monoliths and evaluation of their CO2 capture performance, ACS Appl. Mater. Interfaces 9 (8) (2017) 7489–7498, https://doi.org/10.1021/acsami.6b16732.
[68] M. Naito, T. Yokoyama, K. Hosokawa, K. Nogi, Chapter 2 - Structural control of nanoparticles, Nanoparticle technology handbook (third edition) Chapter 2 - Structural control of nanoparticles (2018) 49-107. https://doi.org/10.1016/B978-0-444-64110-6.00002-0.
[69] V.C.T. Le, M. Sheraz, E. Kang, H.N. Ly, H.D. Mai, A. Anus, S. Kim, Alumina beads decorated copper-based coordination polymer particle filter for commercial indoor air cleaner, Build. Environ. 217 (2022) 109012.
[70] S. Wen, Y. Shen, B. Wen, S. Wu, J. Gu, Z. Zhang, Y. Wei, T. Jiao, Q. Yu, Q. Deng, Y. Chen, Y. Zhao, Enhanced adsorption of aromatic volatile organic compounds on a perchloro covalent triazine framework through multiple intermolecular interactions, Macromol. Rapid Commun. (2023) e2200974.
[71] Y.u. Zhang, Z. Zhu, W.-N. Wang, S.-C. Chen, Mitigating the relative humidity effects on the simultaneous removal of VOCs and PM2.5 of a metal–organic framework coated electret filter, Sep. Purif. Technol. 285 (2022) 120309.
[72] J.-H. Wee, Y. Bae, H. Ahn, Y.O. Choi, E. Jeong, S.Y. Yeo, Fibrous and granular activated carbon mixed media for effective gas removal as a cabin air filter, Carbon Lett. 32 (4) (2022) 1111–1118, https://doi.org/10.1007/s42823-022-00345-7.
[73] K.M. Lee, N.S. Kim, M. Numan, J.C. Kim, H.S. Cho, K. Cho, C. Jo, Postsynthetic modification of zeolite internal surface for sustainable capture of volatile organic compounds under humid conditions, ACS Appl. Mater. Interfaces 13 (45) (2021) 53925–53934, https://doi.org/10.1021/acsami.1c16108.
[74] B. Lei, B. Liu, H. Zhang, L. Yan, H. Xie, G. Zhou, CuO-modified activated carbon for the improvement of toluene removal in air, J. Environ. Sci. 88 (2020) 122–132, https://doi.org/10.1016/j.jes.2019.07.001.
[75] I. Lara-Ibeas, C. Megías-Sayago, B. Louis, S. Le Calvé, Adsorptive removal of gaseous formaldehyde at realistic concentrations, J. Environ. Chem. Eng. 8 (4) (2020) 103986.
[76] I. Pellejero, F. Almazán, M. Lafuente, M.A. Urbiztondo, M. Drobek, M. Bechelany, A. Julbe, L.M. Gandía, Functionalization of 3D printed ABS filters with MOF for toxic gas removal, J. Ind. Eng. Chem. 89 (2020) 194–203, https://doi.org/10.1016/j.jiec.2020.05.013.
[77] S. Wu, Y. Wang, C. Sun, T. Zhao, J. Zhao, Z. Wang, W. Liu, J. Lu, M. Shi, A. Zhao, L. Bu, Z. Wang, M. Yang, Y. Zhi, Novel preparation of binder-free Y/ZSM-5 zeolite composites for VOCs adsorption, Chem. Eng. J. 417 (2021) 129172.
[78] R.M. Serra, L.E. Gómez, I.S. Tiscornia, M.d.L.M. Deharbe, A.V. Boix, CsxCo/Na-MOR coating on ceramic monoliths for co-adsorption of hydrocarbons mixture and selective catalytic reduction of NOx, Catalysts 13 (1) (2023) 106.
[79] J. Lefevere, B. Claessens, S. Mullens, G. Baron, J. Cousin-Saint-Remi, J.F. M. Denayer, 3D-printed zeolitic imidazolate framework structures for adsorptive separations, ACS Appl. Nano Mater. 2 (8) (2019) 4991–4999, https://doi.org/10.1021/acsanm.9b00934.
[80] B. Claessens, N. Dubois, J. Lefevere, S. Mullens, J. Cousin-Saint-Remi, J.F. M. Denayer, 3D-printed ZIF-8 monoliths for biobutanol recovery, Ind. Eng. Chem. Res. 59 (18) (2020) 8813–8824, https://doi.org/10.1021/acs.iecr.0c00453.
[81] S. Couck, J. Cousin-Saint-Remi, S. Van der Perre, G.V. Baron, C. Minas, P. Ruch, J. F.M. Denayer, 3D-printed SAPO-34 monoliths for gas separation, Microporous Mesoporous Mater. 255 (2018) 185–191, https://doi.org/10.1016/j.micromeso.2017.07.014.
[82] X. Lu, T. Ren, P. Cao, Z. Wang, L. Liu, J. He, X.u. Chen, E.F. May, G. Kevin Li, Construction of high performance binder-free zeolite monolith, Chem. Eng. J. 447 (2022) 137558.
[83] T. Chafik, S. Harti, G. Cifredo, J.M. Gatica, H. Vidal, Easy extrusion of honeycomb-shaped monoliths using Moroccan natural clays and investigation of their dynamic adsorptive behavior towards VOCs, J. Hazard. Mater. 170 (1) (2009) 87–95, https://doi.org/10.1016/j.jhazmat.2009.04.127.